High Detectivity and Transparent Few-layer MoS_2/Glassy-Graphene Heterostructure Photodetectors

Hao Xu, Xiaoyu Han, Xiao Dai, Wei Liu, Jiang Wu, Juntong Zhu, Dongyoung Kim, Guifu Zou*, Kimberley A. Sablon, Andrei Sergeev, Zhengxiao Guo, Huiyun Liu**

H. Xu, W. Liu, Dr. J. Wu, D. Kim, Prof. H. Liu
Department of Electronic and Electrical Engineering, University College London
Torrington Place, London WC1E 7JE, United Kingdom
E-mail: jiang.wu@ucl.ac.uk; huiyun.liu@ucl.ac.uk
Dr. X. Han, Prof. Z. Guo
Department of Chemistry, University College London
20 Gordon St, Bloomsbury, London WC1H 0AJ, United Kingdom
Dr. X. Dai, J. Zhu, Prof. G. Zou
College of Physics, Optoelectronics and Energy and Collaborative Innovation Centre of Suzhou Nano Science and Technology
Soochow University, Suzhou 215006, China
E-mail: zouguifu@suda.edu.cn
W. Liu
London Centre for Nanotechnology, University College London
London WC1H 0AH, United Kingdom
Prof. K. A. Sablon, Prof. A. Sergeev
United States Army Research Laboratory
2800 Powder Mill Road, Adelphi, MD 20783-1197, USA

Keywords: glassy-graphene, MoS_2, heterostructures, photodetectors, density functional theory

Abstract

Layered van der Waals heterostructures have attracted considerable attention recently, due to their unique properties both inherited from individual two-dimensional (2D) components and imparted from their interactions. Here, a novel few-layer MoS_2/glassy-graphene heterostructure, synthesised by a layer-by-layer transfer technique, and its application as transparent photodetectors are reported for the first time. Instead of a traditional Schottky

junction, coherent ohmic contact is formed at the interface between the MoS_2 and the glassy-graphene nanosheets. The device exhibits pronounced wavelength selectivity as illuminated by monochromatic lights. A responsivity of 12.3 mA/W and detectivity of 1.8×10^{10} Jones are obtained from the photodetector under 532 nm light illumination. Density functional theory (DFT) calculations reveal the impact of specific carbon atomic arrangement in the glassy-graphene on the electronic band structure. It is demonstrated that the band alignment of the layered heterostructures can be manipulated by lattice engineering of 2D nanosheets to enhance optoelectronic performance.

Main Text

Since the report of graphene and its unique properties in 2004, substantial effort and resources have been devoted to two-dimensional (2D) materials, for their unique properties imparted from surface and quantum confinement effects, compared with the 3D counterparts.[1-3] The 2D family has been considerably enlarged in the last two decades, including, but not limited to, silicene, germanene, stanene, borophene, phosphorene, tellurene, h-boron nitride(h-BN), and transition metal dichalcogenides (TMDs).[3-6] Each holds its own merits and limitations. For example, graphene possesses incomparable electrical and optical properties, which restricts its deployment in electronic and optical devices due to its gapless characteristics.[7, 8] Some single-element 2D materials suffer from instability in air;[4] molybdenum disulfide (MoS_2), as the representative of TMDs, is particularly promising as its monolayer allotrope exhibits a desirable direct band gap of 1.8 eV, which is fitting for both electronic and optoelectronic applications.[9-11] However, it shows relatively low mobility.[12]

To realise the full potential of 2D materials, recent efforts have focused on 2D heterostructures.[13] Among those, graphene/MoS_2 heterostructure is one of the favourable choices, especially for transparent electronic/optoelectronic devices with both aesthetic value

and design flexibility. Despite the successful fabrication of field-effect transistors and photodetectors based on this heterostructure,[14-17] the semi-metal/semiconductor often formed a Schottky junction at the interface, which restricts the performance of 2D device architectures.[18, 19] Hence, heterostructures with tuneable transport properties are highly desirable.

Recently, ultra-smooth cost-effective glassy-graphene (g-graphene) thin films in a large scale (10 cm × 7 cm) have been successfully synthesised.[20] G-graphene is an unique distorted 2D carbon nanosheet distinct from crystalline graphene and largely amorphous glassy carbon, but it possesses intriguing properties such as good transparency (Figure S1), conductivity (Figure S2), flexibility and chemical inertness.[20] Hence, g-graphene adds another dimension of tunability to pristine graphene for practical applications. However, little is known of the prestige properties of the heterostructure of the g-graphene with other 2D materials.

In this paper, we prepared novel few-layer MoS_2/g-graphene heterostructures (MGHs) on quartz substrates using a vertically layer-stacking method. A series of transparent photodetectors were fabricated based on this van der Waals heterostructure and their photoresponsivity exhibited distinct wavelength selectivity, probed by illuminating monochromatic blue, green and red lights, respectively. More importantly, the current-voltage (I-V) characteristics reveal that an ohmic contact was formed between MoS_2 and g-graphene, in contrast to the previously reported Schottky junction between MoS_2 nanosheets and pristine graphene.[14, 16] The photodetectors with different layers of MoS_2 with g-graphene were also compared, where the ohmic contact is insensitive with the thickness of MoS_2. The largest responsivity (12.3 mA/W) and peak detectivity (1.8×10^{10} Jones) were obtained from the device based on the MGH with 3-layer (3L) MoS_2 under illumination of 532 nm monochromatic light. In the periodic photocurrent transient measurements, reproducible device on/off switch was demonstrated. Density functional theory (DFT) calculations were performed to reveal the

mechanism of the ohmic contact at the MGH interface at the atomic level. Detailed discussion on the atomic arrangement of the g-graphene and its effect on the electronic properties was presented, especially the Fermi level and the work function. Compared with the Fermi level and the work function of monolayer MoS_2, the Dirac point of the g-graphene shifts towards the conduction band minimum (CBM) of MoS_2. When an external electrical field is applied on the MGH, the work function was linearly changed. Showing wavelength selectivity and high detectivity, these transparent photodetectors are promising for further integration with electronic/optoelectronic devices, such as touch panels, smart display and sensors.[21, 22]

MoS_2 and g-graphene nanosheets were synthesised by a cost-effective polymer-assisted deposition (PAD) approach on SiO_2/Si and quartz substrates, respectively, as detailed in the supplementary information (SI) and our previous work.[20, 23] A flowchart of the heterostructure synthesis procedure is illustrated in **Figure 1a**. The MoS_2/SiO_2/Si nanosheet was first spin coated with polymethyl-methacrylate (PMMA) and then the PMMA/MoS_2 layer was separated from the SiO_2/Si substrate in a KOH solution. Meanwhile, a g-graphene/quartz nanosheet spin coated with photoresist was patterned by oxygen plasma etching to be the target substrate. Subsequently, the PMMA/MoS_2 was transferred onto the as-treated g-graphene/quartz, followed by the removal of PMMA and cleaning. As can be seen in Figure 1b, the vertically assembled heterostructure on quartz substrate exhibited good transparency. Then, Ti/Au layers were deposited on the MGH as the ohmic contact pads, using an electron-beam evaporator. Figure 1c shows the three-dimensional (3D) schematic view of the transparent photodetector based on the MGH/quartz.

High-resolution transmission electron microscopy (HRTEM) was used to observe the two respective materials for MGHs, **Figure 2a** for MoS_2 and Figure 2b for g-graphene. Both the HRTEM image and the inset of selected-area electron diffraction (SAED) pattern in Figure 2a indicate that the as-grown MoS_2 nanosheets are highly crystalline. Figure 2b shows the

curved and mostly well-crystallised lattice structure of g-graphene but still with distorted planes, which distinguishes g-graphene from glassy carbon and graphene. The SAED pattern of g-graphene shows concentric diffraction rings, indicative of the very fine polycrystalline nature of g-graphene nanosheets. The HRTEM image shows more clearly the rather distinguished atomic ordering: densely populated and closely connected "crystallets" of a few nanometres, which leads to a much more overall structural order than a typical glassy carbon. This unique structure may be attributed to the catalytic re-arrangement of carbon atoms at the local level under the Ni-coating. Figure 2c is an optical image of the MGH/quartz under the microscope. Since the optical contrast of MoS_2 and g-graphene nanosheets on quartz substrate is poor, we can only observe the faint profile of the MGH. Atomic force microscopy (AFM) combined with Raman spectroscopy were used to characterise the pristine MGH. Figure 2d shows the AFM image that was obtained from the circled area in Figure 2c. The surface morphology clearly presents the overlapped area, evidencing the presence of the heterojunction. The inset illustrates the height profile of MoS_2 and g-graphene, which are 1.9 nm and 1 nm, respectively, revealing the trilayer configuration in our MoS_2 nanosheets.[9, 24]

Figure 2e shows the respective Raman spectra of the MGH, as-grown MoS_2 and g-graphene nanosheets obtained under a 532 nm excitation laser. In the Raman spectrum of the MGH, the Raman signatures of both MoS_2 and g-graphene were observed, further confirming the formation of the heterojunction. The two eigen-peaks from MoS_2 in the MGH were clearly observed at 384.8 and 407.8 cm^{-1}, corresponding to the in-plane E^1_{2g} and out-of-plane A_{1g} phonon modes, respectively. The peak wavenumber difference of 23 cm^{-1} between these two Raman modes indicates the MoS_2 nanosheet contains three layers,[25] which is in good agreement with the AFM height profile. Compared with the Raman peaks (D, G, 2D and D+G) obtained from the as-grown g-graphene of 1 nm thick without MoS_2 coverage (the blue curve in Figure 2e), those MGHs show evident changes in the Raman spectrum, including red-shift

frequency and broadened full-width at half maximum (FWHM). This phenomenon could result from an increased electron concentration in the MGH, induced by the photo-excited electrons under the laser illumination.[26]

The transparent photodetectors were electrically characterised under different illumination sources to probe their photoresponsive performance at room temperature, detailed experiment settings listed in the Experimental section. **Figure 3a** presents the I-V curve of the device based on 3L MoS_2/1 nm g-graphene under AM 1.5G one sun illumination. Compared with the dark current, the photo-induced current was increased by almost 50% and continued to increase with the bias voltage. It is worth noting that both the dark current and photo-induced current measured between the respective contacts located on MoS_2 and g-graphene ends show a symmetrically linear dependence on the applied bias voltage. The same I-V relationship was found for the device based on 9L MoS_2/6 nm g-graphene (the material characterisation results are presented in Figure S4 – S6) as well (see Figure 3b). As shown in our previously study, the g-graphene nanosheets of different thicknesses share similar properties.[20] The linear behaviour indicates an ohmic contact was formed at the interface between MoS_2 and g-graphene, unlike the previously reported Schottky junction features in MoS_2/graphene heterostructures.[14-17] Photocurrent ($I_{pc} = I_{illumination} - I_{dark}$) vs. voltage characteristics of photodetectors under illumination of monochromatic blue (λ: 405 nm), green (λ: 532 nm) and red (λ: 656 nm) lights are shown in Figures 3c and 3d. Due to the good transparency and smoothness of devices, especially for the one based on the MGH with 3L MoS_2, most of light was reflected or transmitted during the irradiating process, and the energy loss, for instance, can reach to as high as 94.5% for the blue light. Nonetheless, the incident lights of these three different wavelengths were still detected with different I_{pc} which all linearly depend on the applied bias voltage. For the device with 3L MoS_2, the red light exited the most photoelectrons, while the largest I_{pc} was generated by the blue light for the device with 9L MoS_2.

To understand this ohmic behaviour of the heterostructure, *i.e.* linear dependence of dark current and photocurrent with bias voltage, theoretical calculations were carried out based on DFT. According to the HRTEM image (Figure 2b) and the Raman peaks (Figure 2e) of the g-graphene, it is an ambitious challenge to model the g-graphene structure at the DFT level, detailed analysis in the SI. Among all the defect forms in graphene, the Stone-Wales (SW) defect, formed by twisting the C-C bond by 90º (see Figure S7), is the only one without atom missed or added, compared with crystal structures of pristine graphene.[27] Based on the synthesis of g-graphene and graphene procedure, the coated Ni film catalysed *in-situ* the carbon crystallinity and confinement at different annealing temperatures.[20] Hence, those carbon atoms rearrangement in g-graphene should be dominant by the SW defects, which was adopted to represent the g-graphene in our study.

The formation energy of different defect concentration (Figure S8) models was calculated based on $E_f = E_{n\times n}(SW) - E_{n\times n}(pristine)$, where $E_{n\times n}$(SW) and $E_{n\times n}$(pristine) are the energy of $n \times n$ supercell with and without the SW defects, respectively. The foreseeable results were shown in Table S1, where the defect formation energy decreases with the values of the defect concentration. Moreover, the random defect structural arrangement was carried out using the 8×8 supercell, with one, two, and maximum SW defects appeared in the supercell (see **Figure 4b** – 4d), compared with pristine graphene (Figure 4a). These configurations, with one, two and maximum SW defects in the systems were denoted as g-graphene-(1), g-graphene-(2) and g-graphene-(max), respectively. Compared with the band structure of pristine graphene (**Figure 5a**), a bandgap emerged at the Dirac point of those with SW defects, and the width of the gap increases with the value of the defect ratio, as shown in Figures 5b and 5c. The corresponding band structure at the K point shows that the linear dispersion has been preserved, as shown in the inserted Figures 5b and 5c. Hence, a small bandgap could be expected at the g-graphene with relatively high electron/hole conductivity.

This is one of the main reasons for the high responsivity of the MGH photodetectors. Further, the density of states (DOS) of the g-graphene-(1) (Figure 4b), was plotted in Figure 4e, where the valence band maximum (VBM) almost meets the CBM, with a band gap of 0.03 eV at the Dirac point (Figure 5e). Projected density of states (pDOS) reveals the atomic level characteristics of the CBM and VBM of the materials. For the single SW defect (see Figures 4b and S9), the contribution of the two twisted atoms (the grey balls) and the rest in the 5-member (the blue and pink balls) and the 7-member (the dark red and pink balls) rings were shown in Figures 4f – 4h, respectively. The two twisted atoms contribute most to the CBM and VBM, dominated by p_z orbitals, which will further influence the heterostructure with MoS_2. It should be expected that the CBM and VBM of the g-graphene are largely contributed by those twisted C-C bond atoms.

Since graphene is nearly 3.7 times stiffer than monolayer MoS_2,[28, 29] the hybrid supercell, shown in Figure 5d, was built over graphene by adjustment of MoS_2. Hence, the supercells consist of $\sqrt{21} \times \sqrt{21}\, R16.10°$ of MoS_2 and 8×8 of graphene/g-graphene. The lattice mismatch is only 0.59%. To demonstrate the electrical properties of the g-graphene/MoS_2 heterostructures, g-graphene-(2)/MoS_2 was selected as a representative. By applying an external electrical field, the work function responds lineally to the external electrical field, as shown in Figure 5e. Meanwhile, the Fermi level drops accordingly. This linear response can originate from the band alignments of the g-graphene and MoS_2. The work functions of graphene, g-graphene-(1), g-graphene-(2) and g-graphene-(max) were listed in Table S2. The work function is the lowest for the perfect graphene, and then seems to increase with the concentration of defects. Compared with the band structure of MoS_2, shown in Figure 5f, the pristine graphene shows a relatively low work function, compared with the CBM of MoS_2, which fundamentally creates a Schottky barrier with the MoS_2 hybrid. The Dirac point of the g-graphene-(max) is below the CBM of MoS_2. Hence, the Dirac point of the as-

synthesised g-graphene should more or less match the CBM of the MoS_2. Moreover, as observed experimentally,[30] the majority charge transport of the MoS_2 heterostructure is dominated by electrons rather than thermionic emission. Hence, only the location of the CBM of the MoS2 need to be considered. When an external electrical field is applied, electrons at the conduction band could experience barrierless transfer from g-graphene to MoS_2, and hence an ohmic contact was formed between the g-graphene and MoS_2.

To further understand the nature of interfaces, we further calculated the charge difference of the g-graphene (2) /MoS_2 as a representative, compared with the pristine graphene/MoS_2. As shown in **Figure 6**(b, d), the charge redistribution of g-graphene(2)/MoS_2 heterostructure is smooth and straightforward, only involving the S atoms with the nearby C atoms, which forms the electron transfer tunnels. This newly formed tunnel could be the reason that the junction property of the heterostructure is insensitive to the thickness of the MoS_2 observed in our experiment. Whereas the charge redistribution between the perfect graphene and MoS_2 are more significant, Figure 6(a, c). This implies that the electron potential oscillates between the interface, which can induce the vdW gap.[31,32]

Corresponding photoresponsivity (R_A, defined as $R_A = I_{pc}/P$, here P denotes incident optical power) of the photodetectors was calculated, and plotted in **Figures 7a** and 7b as a function of the applied voltage. The largest R_A of 12.3 mA/W was recorded as the device of 3L MoS_2 was illuminated by green light at a bias voltage of 1V (see Figure 7a). For the red and blue lights, the R_A is 1.2 mA/W and 0.07 mA/W when the device was at a biased voltage of 1V, respectively. Under similar experimental setup, the R_A of our photodetector is higher than that of graphene based photodetector (0.25 mA/W),[33] monolayer MoS_2 based phototransistor (0.42 mA/W) and photosensor (1.1 mA/W).[10, 34] The high responsivity demonstrated in this work can be attributed to fast transfer and collection of photocarriers from MoS_2 to g-graphene. In addition, it is apparent that the device exhibits varying R_A with orders of magnitude difference

to different monochromatic lights. This marked wavelength selectivity was repeated for the device with 9L MoS_2 as well (see Figure 7b), in which the respective R_A is 0.65, 0.07 and 0.01 mA/W for green, red and blue lights, respectively. Both devices show the best photodetection capability for 532 nm light and are also suitable for detecting 656 and 405 nm lights, which was achieved without applying a gate voltage. The photoresponsive performance of the device with 3L MoS_2 was superior to that with 9L MoS_2, which may result from a higher defect density in the 9L MoS_2, as noted in the AFM image, Figure S5. Additionally, power-dependent photocurrent of the MGH devices were measured. Both the photocurrent of both devices increased with increase in excitation intensity. The photocurrent measured as a function of excitation power is shown in Figure 7e. While a typical linear behaviour of the photocurrent is observed for the 3ML MoS_2 MGH photoconductor, the 9 ML MoS_2 MGH device shows a clear non-linear trend. This non-unity exponent confirms the existence of carrier traps in the thicker MoS_2 nanosheets.

Specific detectivity (D^*), as another significant figure of merit for photodetectors, is given by the following: $D^* = R(A/2qI_{dark})^{1/2}$, where A is the effective area of the device and q is the elementary charge. Due to the large R_A and relatively low dark current, a high D^* of 1.8×10^{10} Jones was attained for 532 nm light, which is comparable to the MoS_2/graphene heterostructure based devices (1.5×10^{10} Jones for 520 nm light) and multilayer MoS_2 phototransistors ($\sim10^{10}$ Jones for 532 nm light).[35, 36]

We then explored the photocurrent under on/off switching as a function of time when applying a constant bias voltage of 1 V to devices, as shown in Figures 7c and 7d. In Figure 7c, the device responded to the green and red lights with an increasing photocurrent, showing traditional positive photoresponse. However, negative photoresponse at room temperature was observed in the device under the blue light illumination, i.e. the value of the photocurrent decreased as measurement time increased as shown in Figure 3c. Combining with the analysis

of photocurrent measured under the linear voltage sweeping (the blue curve shown in Figure 3c), we find that the photoconductivity of the device can either increase or decrease under the 405 nm light illumination, which was also reported in the metal-nanoparticle-based materials and doped graphene photodetectors.[21, 37] This behaviour could be due to the disorder-related localised states in g-graphene and especially pronounced in low dimensional materials.[38, 39] In Figure 7d, similarly, the device exhibits conventional transient photoresponse. The slow rising and falling time of the photocurrent, on the one hand, could arise from the islands on the surface of MoS_2 (as shown in Figure 2d) which can trap a large number of photo-excited electrons.[40] On the other hand, it could be due to the surrounding impacts (including substrates, contact metals, *etc*.) on the photo-induced current dynamics.[41] Despite the slow response time, both figures demonstrate the reproducibility of our devices.

In summary, transparent photodetectors based on novel few-layer MGHs with high detectivity were fabricated for the first time. An ohmic contact was formed at the interface between MoS_2 and g-graphene, instead of the traditional Schottky junction, leading to marked improvement of charge transfer for future 2D devices. The photodetectors exhibited distinct wavelength selectivity. Despite good transparency, these devices also show high absorption in contrast with pure graphene of which the absorption is negligible. The device with 3L MoS_2 exhibited the largest responsivity of 12.3 mA/W and detectivity of 1.8×10^{10} Jones under 532 nm light illumination, regardless of the large incident optical power loss. Transient photocurrent dynamics showed the reproducible on/off switch of the devices. Theoretical calculations revealed that defects have different impacts on the conduction and valence band. Increasing the defect concentration further opens a band gap at the Dirac point, where the linear dispersion was well preserved to ensure high mobility of charge carriers. Meanwhile, the Dirac point of g-graphene shifted towards the CBM of MoS_2. In addition, the linear response of the work function and Fermi level of g-graphene/MoS_2 heterostructure under external electrical

field also demonstrated the ohmic behaviour at the interface. The unique tunability of the electronic band structure of the g-graphene/MoS_2 heterostructure opens new opportunities for design and fabrication of 2D devices.

Experimental Section

MGH preparation: Figure 1a shows the procedures involved to prepare the MGH. PMMA was spin coated onto $MoS_2/SiO_2/Si$ at 4000 rpm for 60 s and then baked at 180 °C for 2 minutes. PMMA-covered MoS_2 was separated from the SiO_2/Si substrate by 1 M KOH solution at 80 °C and then transferred into deionised water. The photoresist was spin coated onto g-graphene/quartz at 6000 rpm for 60 s followed by baking at 115 °C for 1 minute. After standard ultraviolet photolithography processing, g-graphene was patterned by oxygen plasma etching in Diener Plasma Asher for 1 minute. As-treated g-graphene was used as the target substrate and immersed into the deionised water to attach the PMMA-covered MoS_2. Afterwards, the MGH was baked at 180 °C for 5 minutes and then soaked into acetone to dissolve the PMMA.
Material characterisation: HR-TEM and AFM measurements were carried out in a FEI Tecnai F20 system and Veeco Dimension V Scanning Probe Microscope with tapping mode in the air, respectively. Optical microscope images were obtained using an Olympus Reflection Microscope. Raman spectroscopy was performed in a Renishaw inVia micro-Raman system using a 532 nm excitation laser and 1800 g/mm^2 grating through a ×50 objective lens. The laser power was controlled at about 1 mW.
Photodetector fabrication: Photoresist was spin coated onto MGH/quartz at 6000 rpm for 60 s and subsequently baked at 115 °C for 1 minute. Ti/Au (10 nm/50 nm) contact pads were formed by standard ultraviolet photolithography, electron-beam evaporator deposition and lift-off techniques. Afterwards, the devices were wire-bonded using gold wires to the chip carriers for

measurements. The size of overlapped area (the heterojunction) between MoS2 and g-graphene is approximately 1 mm by 2 mm, and the size of metal contact pad is approximately 1 mm by 1 mm. MoS_2 acts as the absorber and glassy graphene as the transparency electrode.

Device characterisation: The electrical measurement under illumination was conducted using a Keithley 4200 semiconductor parameter analyser. Three lasers were added as the illumination sources at the ambient condition. The lasers are unfocused and the spot size is estimated to be 1 mm in diameter. The corresponding effective power for red, green and blue laser was controlled at 10.3, 0.8 and 92.2 μW, respectively.

DFT calculation: All the calculations were carried out based on Density Functional Theory (DFT), implanted in Vienna *ab initio* Package (VASP).[42] The Perdew-Burke-Ernzerhof (PBE) function for the exchange-correlation term was used with the projector augmented wave method.[43, 44] A plane wave cut-off of 500 eV was set with forces converged to 0.01 eV/Å. K-points was sampled by 7×7×1 for relaxation and 15×15×1 for project Density of States (pDOS). A 15 Å vacuum slab was added for each model to prevent periodic interaction. Semi-core *p* states of molybdenum were also considered as the valence states. Dipole correction has been considered through the whole calculations. The DFT-D2 method of Grimme was employed for the van der Waals correction.[45]

A series of models, 4×4, 5×5, 6×6, 7×7 and 8×8 supercells, were carried out based on different Stone-Wales defect ratios, representing g-graphene. Moreover, the defects were also tested in the random position in the 8×8 supercell, with the extreme case g-graphene-(max) where only one six-member ring was surrounded by either five- or seven-member rings. For MoS_2, our optimised lattice parameters of monolayer and bulk are 3.183 Å and 3.202 Å, respectively, which are in line with previous experimental observations.[46, 47]

Supporting Information

Supporting Information is available from the Wiley Online Library or from the author.

Acknowledgements

H. X., X. H. and X. D. contributed equally to this work. This work was supported by grants from the UK EPSRC Future Compound Semiconductor Manufacturing Hub (EP/P006973/1). The authors would also like to thanks to the financial support by EPSRC (EP/L018330/1) and acknowledge the use of the UCL Grace High Performance Computing Facility (Grace@UCL) and associated support services, in completion of this work. In addition, we acknowledge the support from the U.S. Army Research Laboratory under Cooperative Agreement Number W911NF-16-2-0120, the "973 Program—the National Basic Research Program of China" Special Funds for the Chief Young Scientist (2015CB358600), the Excellent Young Scholar Fund from National Natural Science Foundation of China (21422103), and the China Scholarship Council (CSC).

Conflict of Interest

The authors declare no conflict of interest.

References

[1] K. S. Novoselov, A. K. Geim, S. V. Morozov, D. Jiang, Y. Zhang, S. V. Dubonos, I. V. Grigorieva, A. A. Firsov, *Science.* **2004**, *306*, 666.

[2] F. Xia, H. Wang, D. Xiao, M. Dubey, A. Ramasubramaniam, *Nat. Photonics* **2014**, *8*, 899.

[3] A. Castellanos-Gomez, *Nat. Photonics* **2016**, *10*, 202.

[4] A. J. Mannix, B. Kiraly, M. C. Hersam, N. P. Guisinger, *Nat. Rev. Chem.* **2017**, *1*, 0014.

[5] Y. Wang, G. Qiu, Q. Wang, Y. Liu, Y. Du, R. Wang, W. A. Goddard, M. J. Kim, P. D. Ye, W. Wu, *arXiv Prepr. arXiv* **2017**, *1704*, 06202.

[6] K. F. Mak, J. Shan, *Nat. Photonics* **2016**, *10*, 216.

[7] F. Schwierz, *Nat. Nanotechnol.* **2010**, *5*, 487.

[8] Z. Yin, J. Zhu, Q. He, X. Cao, C. Tan, H. Chen, Q. Yan, H. Zhang, *Adv. Energy Mater.* **2014**, *4*, 1.

[9] B. Radisavljevic, A. Radenovic, J. Brivio, V. Giacometti, A. Kis, *Nat. Nanotechnol.* **2011**, *6*, 147.

[10] Z. Yin, H. Li, H. Li, L. Jiang, Y. Shi, Y. Sun, G. Lu, Q. Zhang, X. Chen, H. Zhang, *ACS Nano* **2012**, *6*, 74.

[11] M. L. Tsai, S. H. Su, J. K. Chang, D. S. Tsai, C. H. Chen, C. I. Wu, L. J. Li, L. J. Chen, J. H. He, *ACS Nano* **2014**, *8*, 8317.

[12] S. Xu, Z. Wu, H. Lu, Y. Han, G. Long, X. Chen, T. Han, W. Ye, Y. Wu, J. Lin, J. Shen, Y. Cai, Y. He, F. Zhang, R. Lortz, C. Cheng, N. Wang, *2D Mater.* **2016**, *3*, 021007.

[13] A. K. Geim, I. V. Grigorieva, *Nature* **2013**, *499*, 419.

[14] H. Tian, Z. Tan, C. Wu, X. Wang, M. A. Mohammad, D. Xie, Y. Yang, J. Wang, L.-J.

Li, J. Xu, T.-L. Ren, *Sci. Rep.* **2014**, *4*, 5951.

[15] P. Vabbina, N. Choudhary, A.-A. Chowdhury, R. Sinha, M. Karabiyik, S. Das, W. Choi, N. Pala, *ACS Appl. Mater. Interfaces* **2015**, *7*, 15206.

[16] J. Y. Kwak, J. Hwang, B. Calderon, H. Alsalman, N. Munoz, B. Schutter, M. G. Spencer, *Nano Lett.* **2014**, *14*, 4511.

[17] W. J. Yu, Z. Li, H. Zhou, Y. Chen, Y. Wang, Y. Huang, X. Duan, *Nat. Mater.* **2013**, *12*, 246.

[18] A. Allain, J. Kang, K. Banerjee, A. Kis, *Nat. Mater.* **2015**, *14*, 1195.

[19] D. Jena, K. Banerjee, G. H. Xing, *Nat. Mater.* **2014**, *13*, 1076.

[20] X. Dai, J. Wu, Z. Qian, H. Wang, J. Jian, Y. Cao, M. H. Rummeli, Q. Yi, H. Liu, G. Zou, *Sci. Adv.* **2016**, *2*, 1.

[21] N. Liu, H. Tian, G. Schwartz, J. B. H. Tok, T. L. Ren, Z. Bao, *Nano Lett.* **2014**, *14*, 3702.

[22] H. Zhang, S. Jenatsch, J. De Jonghe, F. Nüesch, R. Steim, A. C. Véron, R. Hany, *Sci. Rep.* **2015**, *5*, 9439.

[23] J. Zhu, J. Wu, Y. Sun, J. Huang, Y. Xia, H. Wang, H. Wang, Y. Wang, Q. Yi, G. Zou, *RSC Adv.* **2016**, *6*, 110604.

[24] D.-S. Tsai, K.-K. Liu, D.-H. Lien, M.-L. Tsai, C.-F. Kang, C.-A. Lin, L.-J. Li, J.-H. He, *ACS Nano* **2013**, *7*, 3905.

[25] H. Li, Q. Zhang, C. C. R. Yap, B. K. Tay, T. H. T. Edwin, A. Olivier, D. Baillargeat, *Adv. Funct. Mater.* **2012**, *22*, 1385.

[26] a Das, S. Pisana, B. Chakraborty, S. Piscanec, S. K. Saha, U. V Waghmare, K. S. Novoselov, H. R. Krishnamurthy, a K. Geim, a C. Ferrari, a K. Sood, *Nat. Nanotechnol.* **2008**, *3*, 210.

[27] F. Banhart, J. Kotakoski, A. V. Krasheninnikov, *ACS Nano* **2011**, *5*, 26.

[28] C. Lee, X. Wei, J. W. Kysar, J. Hone, *Science.* **2008**, *321*, 385.

[29] S. Bertolazzi, J. Brivio, A. Kis, *ACS Nano* **2011**, *5*, 9703.

[30] C. Kim, I. Moon, D. Lee, M. S. Choi, F. Ahmed, S. Nam, Y. Cho, H.-J. Shin, S. Park, and W. J. Yoo, *ACS Nano* **2017**, 11, 1588.

[31] A. Allain, J. Kang, K. Banerjee, A. Kis, *Nat. Materials* **2015**, 14, 1195-1205.

[32] Y. Du, L. Yang, J. Zhang, H. Liu, K. Majumdar, P. D. Kirsch, and P. D. Ye, IEEE *Electron Device Lett.* **2014**, 35, 599-601.

[33] M. Freitag, T. Low, F. N. Xia, P. Avouris, *Nat. Photonics* **2013**, *7*, 53.

[34] N. Perea-López, Z. Lin, N. R. Pradhan, A. Iñiguez-Rábago, A. Laura Elías, A. McCreary, J. Lou, P. M. Ajayan, H. Terrones, L. Balicas, M. Terrones, *2D Mater.* **2014**, *1*, 011004.

[35] S. Rathi, I. Lee, D. Lim, J. Wang, Y. Ochiai, N. Aoki, K. Watanabe, T. Taniguchi, G.-H. Lee, Y.-J. Yu, P. Kim, G.-H. Kim, *Nano Lett.* **2015**, *15*, 5017.

[36] W. Choi, M. Y. Cho, A. Konar, J. H. Lee, G. B. Cha, S. C. Hong, S. Kim, J. Kim, D. Jena, J. Joo, S. Kim, *Adv. Mater.* **2012**, *24*, 5832.

[37] H. Nakanishi, K. J. M. Bishop, B. Kowalczyk, A. Nitzan, E. A. Weiss, K. V Tretiakov, M. M. Apodaca, R. Klajn, J. F. Stoddart, B. A. Grzybowski, *Nature* **2009**, *460*, 371.

[38] C. Biswas, F. Güneş, D. D. Loc, S. C. Lim, M. S. Jeong, D. Pribat, Y. H. Lee, *Nano Lett.* **2012**, *12*, 6505.

[39] M. Liao, Y. Koide, J. Alvarez, M. Imura, J. P. Kleider, *Phys. Rev. B - Condens. Matter Mater. Phys.* **2008**, *78*, 1.

[40] K. Dolui, I. Rungger, S. Sanvito, *Phys. Rev. B - Condens. Matter Mater. Phys.* **2013**, *87*, 1.

[41] O. Lopez-Sanchez, D. Lembke, M. Kayci, A. Radenovic, A. Kis, *Nat. Nanotechnol.* **2013**, *8*, 497.

[42] G. Kresse, J. Furthmüller, *Comput. Mater. Sci.* **1996**, *6*, 15.

[43] J. P. Perdew, K. Burke, M. Ernzerhof, *Phys. Rev. Lett.* **1996**, *77*, 3865.

[44] P. E. Blöchl, *Phys. Rev. B* **1994**, *50*, 17953.

[45] S. Grimme, *J. Comput. Chem.* **2006**, *27*, 1787.

[46] P. a Young, *J. Phys. D. Appl. Phys.* **1968**, *1*, 936.

[47] S. Helveg, J. Lauritsen, E. Laegsgaard, I. Stensgaard, J. Norskov, B. Clausen, H. Topsoe, F. Besenbacher, *Phys. Rev. Lett.* **2000**, *84*, 951.

Figure 1. Schematic of MGH preparation and 3D view of the transparent photodetector. a) Preparation procedures of the few-layer MGH. b) Digital photograph showing the transparent and large-scale MGH/quartz. c) 3D model of the transparent photodetector based on the MGH/quartz.

Figure 2. Material characterisations of the MGH, as-grown MoS_2 and g-graphene nanosheets. HRTEM images and SAED patterns (insets) of: a) PAD-synthesised MoS_2, and b) g-graphene nanosheets, respectively; c) Optical microscope image of the MGH; d) AFM image obtained from the area labelled by the red circle in c) and the inset showing the height profile along the red line; e) Raman spectra of the MGH, as-grown $MoS_2/SiO_2/Si$ and g-graphene/quartz nanosheets, respectively. The Raman spectrum of the MGH was taken at the heterojunction area within the red circle of Figure 2c. The two green curves represent fitted peaks of 2D and D+G, and the olive one represents the fitting curve.

Figure 3. Photoresponsive performance characterisation of photodetectors under different illuminations. a, b) I-V characteristic curves of devices based on the MGHs with 3L and 9L MoS_2 in the dark and under AM 1.5G illumination, respectively. c, d) Photocurrent transfer curves of devices based on the MGHs with 3L and 9L MoS_2 under monochromatic blue, green and red lights, respectively. The inset in c) shows a device under testing with a green laser.

Figure 4. The structural configurations of graphene with different defect ratios in an 8×8 supercell: a) the pristine graphene, g-graphene with b) one, c) two and d) maximum SW defects, respectively. The DOS of single SW configuration and pDOS of different atoms in this configuration: e) The DOS of g-graphene with a single SW defect. f) pDOS of the two atoms twisting the C-C bond by 90º (the grey balls in Figure S9). g) pDOS of the rest atoms

composing 5-member rings (the blue and pink balls in Figure S9). h) pDOS of the rest atoms composing 7-member rings (the dark red and pink balls in Figure S9).

Figure 5. The band structures of (a) graphene, (b) g-graphene-(1) and (c) g-graphene-(2), respectively. Inset: a zoom-in view of the band structure at the K point as indicated in dashed boxes in Figure 5a – 5c, respectively. (d) Top-view of graphene/MoS_2 heterostructure, which consists 8×8 and $\sqrt{21} \times \sqrt{21}$R16.10° of graphene and MoS_2, respectively. (e) The work function and Fermi level of g-graphene-(2)/MoS_2 heterostructure in response to an external electrical field. (f) The band alignment of g-graphene and MoS_2.

Figure 6. Top views (a) and (b) are charge differences of the perfect graphene /MoS_2, and the g-graphene(2)/MoS_2, respectively. The corresponding side views are given in (c) and (d), respectively. All the isosurface is set to $0.0002e/a_0^3$, where a_0 is the Bohr radius. The yellow and blue regions represent charge accumulation and reduction, respectively.

Figure 7. Photoresponsivity and time-resolved photoresponse of photodetectors under different illuminations. a, b) Photoresponsivity of devices with 3L MoS_2 and 9L MoS_2 as illuminated by monochromatic blue, green and red lights, respectively. c, d) Photo-induced current dynamics of devices with 3L MoS_2 and 9L MoS_2 as illuminated by monochromatic blue, green and red lights, respectively. The applied constant voltage is 1 V. The time gap between on/off switching is 20 s. (e) Intensity dependent photocurrent at the bias voltage of 1 V and corresponding power-law fitting of MGH devices under 656 nm light illumination. The data points at zero incident power are the dark currents.

Figure 1.

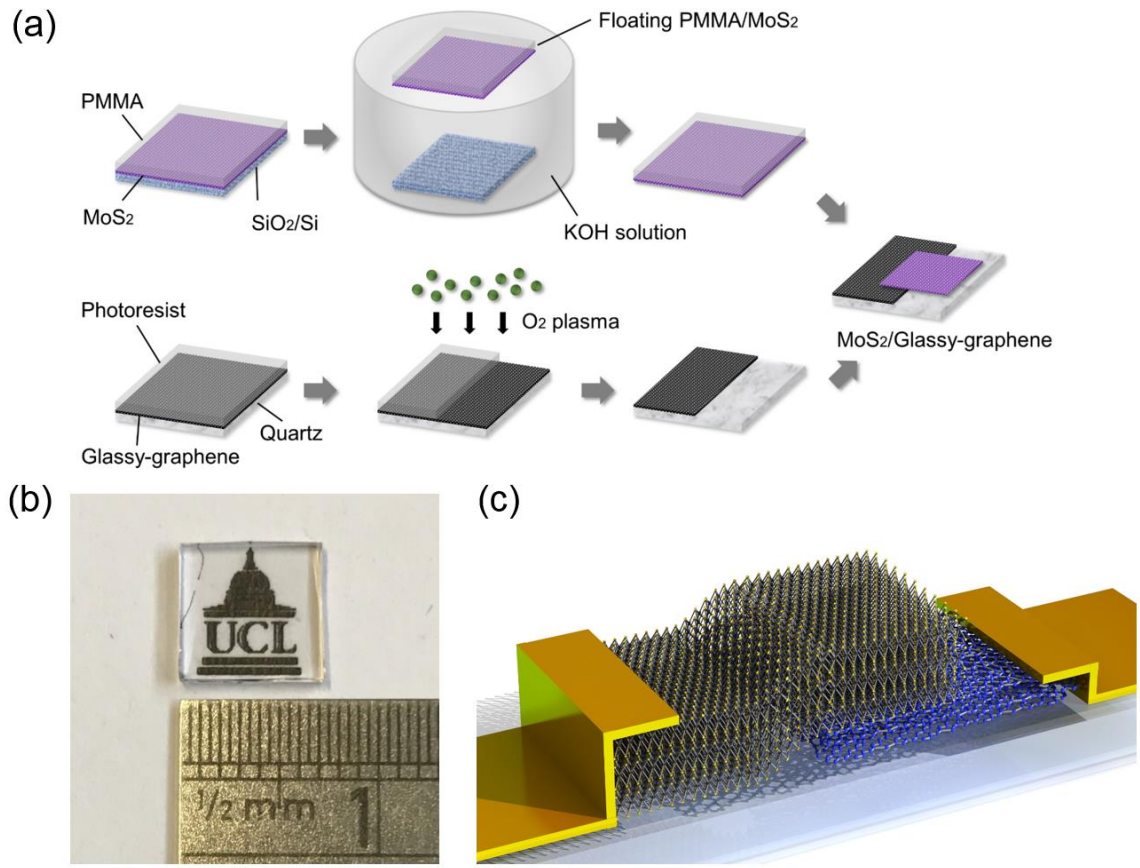
(a)
PMMA
MoS2
SiO2/Si
Floating PMMA/MoS2
KOH solution
MoS2/Glassy-graphene
Photoresist
Glassy-graphene
Quartz
O2 plasma
(b)
UCL
1/2 mm
1
(c)

Figure 2.

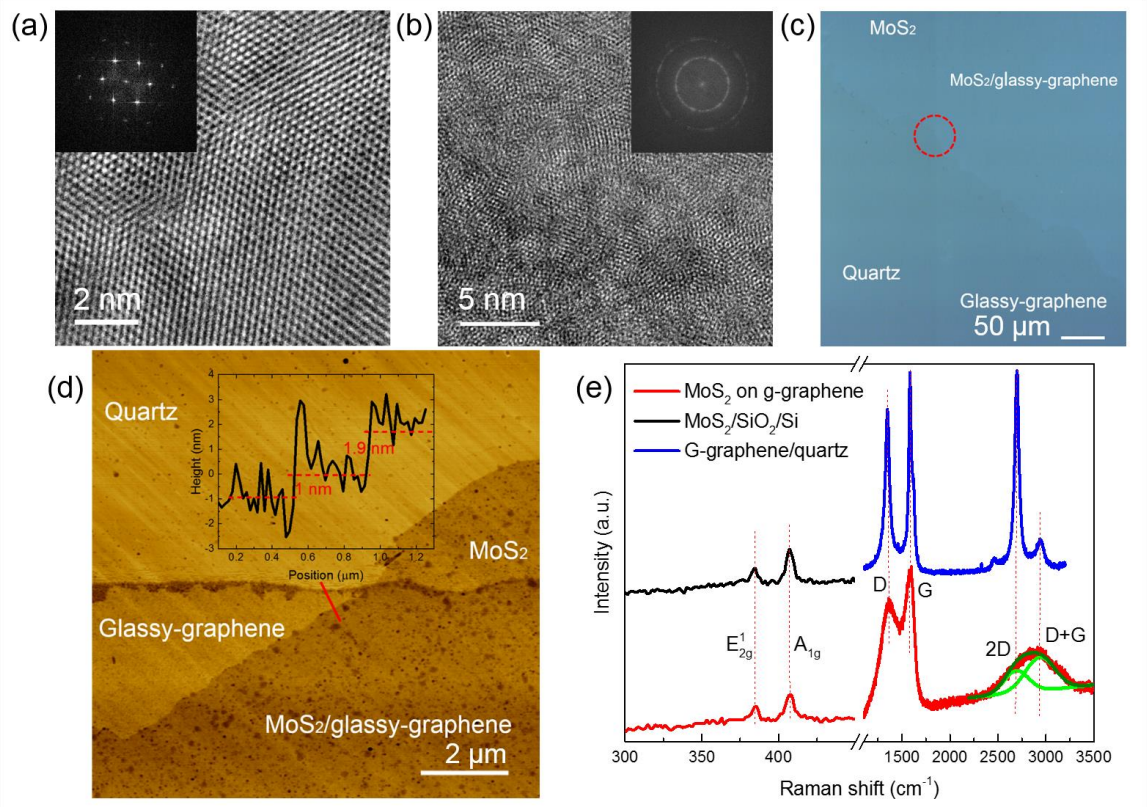
(a)
2 nm
(b)
5 nm
(c)
MoS2
MoS2/glassy-graphene
Quartz
Glassy-graphene
50 μm
(d)
Quartz
Height (nm)
1.9 nm
1 nm
Position (μm)
MoS2
Glassy-graphene
MoS2/glassy-graphene
2 μm
(e)
MoS2 on g-graphene
MoS2/SiO2/Si
G-graphene/quartz
Intensity (a.u.)
D
G
E12g
A1g
2D
D+G
Raman shift (cm-1)

Figure 3.

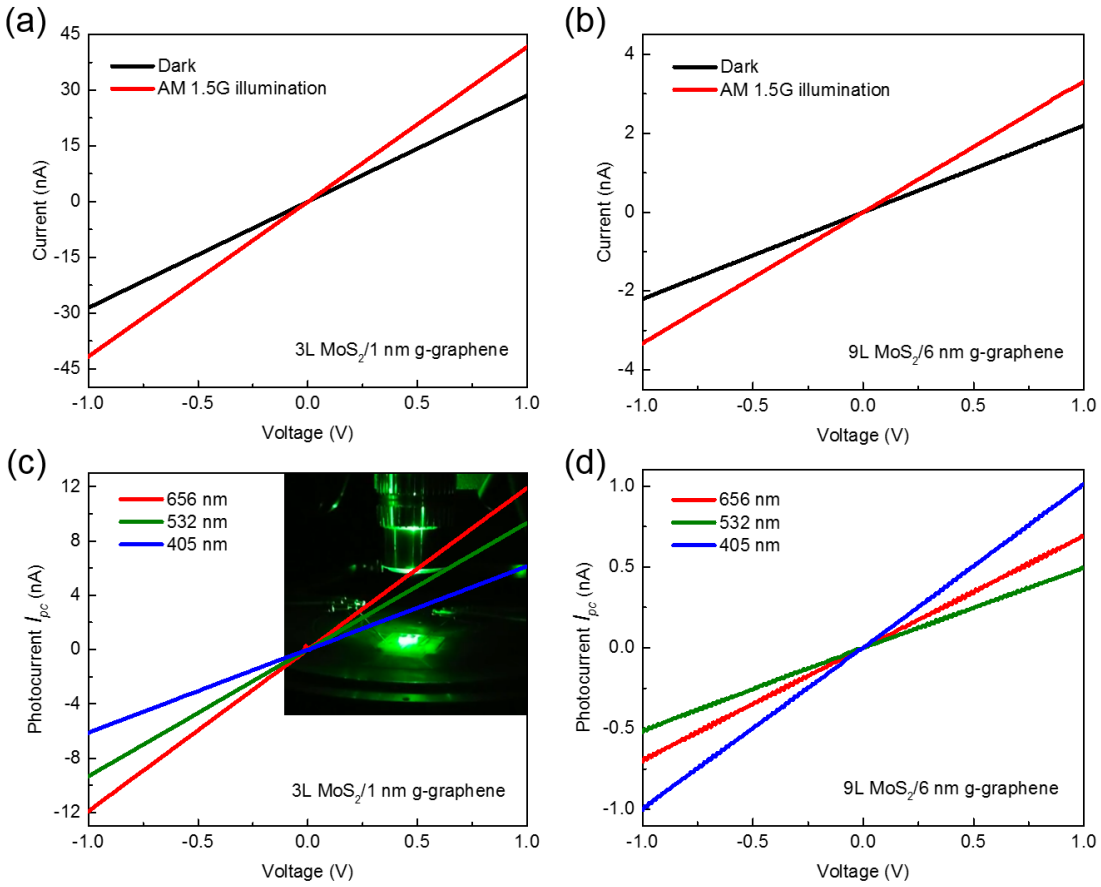
(a)
Dark
AM 1.5G illumination
Current (nA)
Voltage (V)
3L MoS2/1 nm g-graphene
(b)
Dark
AM 1.5G illumination
Current (nA)
Voltage (V)
9L MoS2/6 nm g-graphene
(c)
656 nm
532 nm
405 nm
Photocurrent Ipc (nA)
Voltage (V)
3L MoS2/1 nm g-graphene
(d)
656 nm
532 nm
405 nm
Photocurrent Ipc (nA)
Voltage (V)
9L MoS2/6 nm g-graphene

Figure 4.

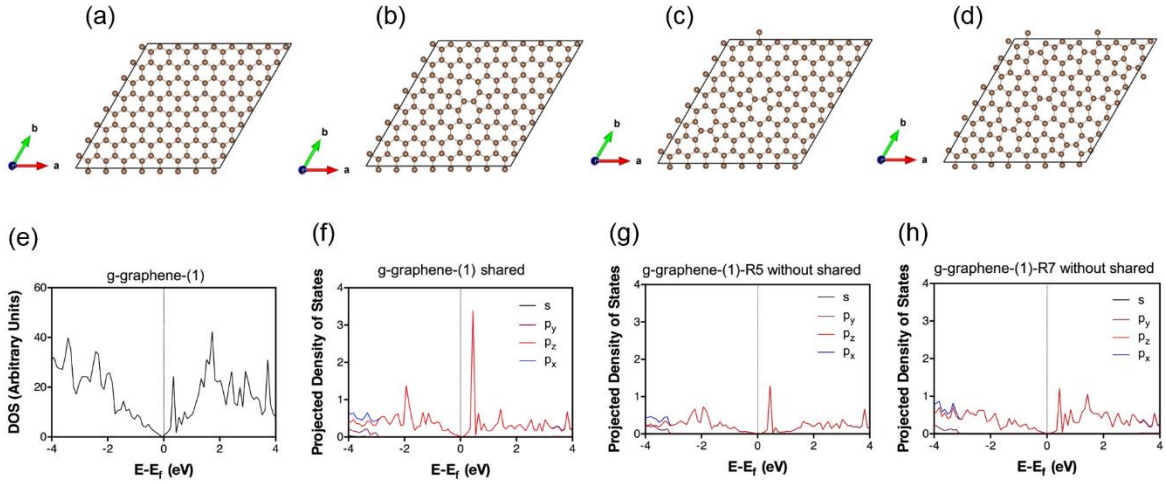
(a)
(b)
(c)
(d)
b
a
(e)
g-graphene-(1)
DOS (Arbitrary Units)
E-E$_f$ (eV)
(f)
g-graphene-(1) shared
Projected Density of States
s
p$_y$
p$_z$
p$_x$
E-E$_f$ (eV)
(g)
g-graphene-(1)-R5 without shared
Projected Density of States
s
p$_y$
p$_z$
p$_x$
E-E$_f$ (eV)
(h)
g-graphene-(1)-R7 without shared
Projected Density of States
s
p$_y$
p$_z$
p$_x$
E-E$_f$ (eV)

Figure 5.

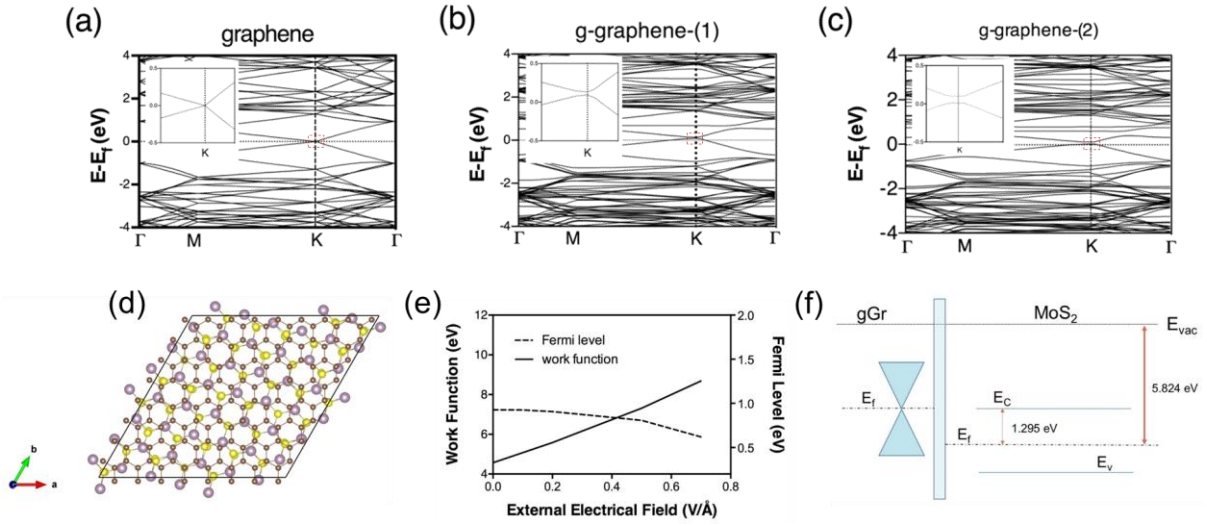
(a)
graphene
(b)
g-graphene-(1)
(c)
g-graphene-(2)
E-E$_f$ (eV)
Γ M K Γ
K
(d)
b
a
(e)
Fermi level
work function
Work Function (eV)
Fermi Level (eV)
External Electrical Field (V/Å)
(f)
gGr
MoS$_2$
E$_{vac}$
E$_f$
E$_C$
1.295 eV
5.824 eV
E$_v$

Figure 6.

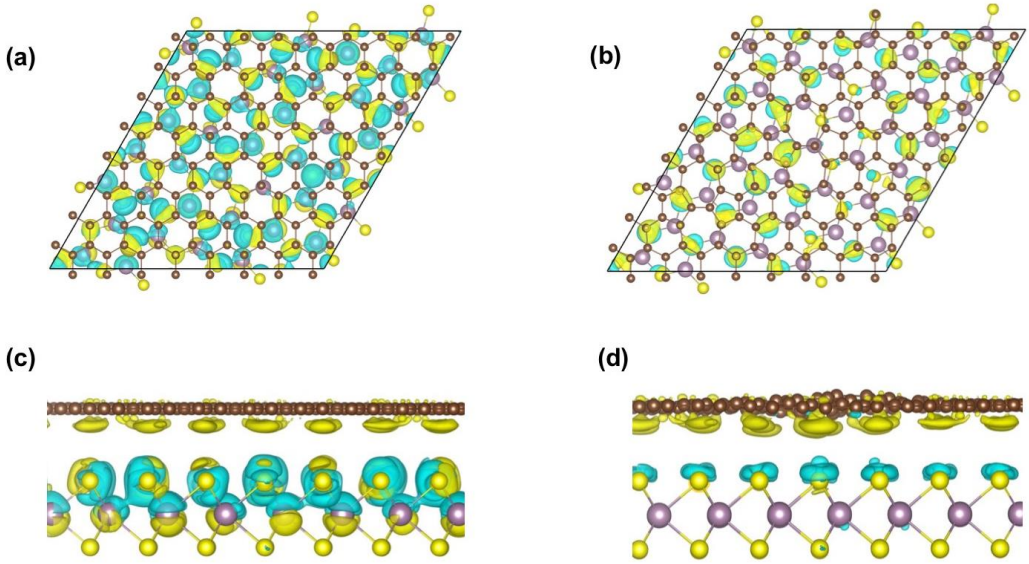

Figure 7.

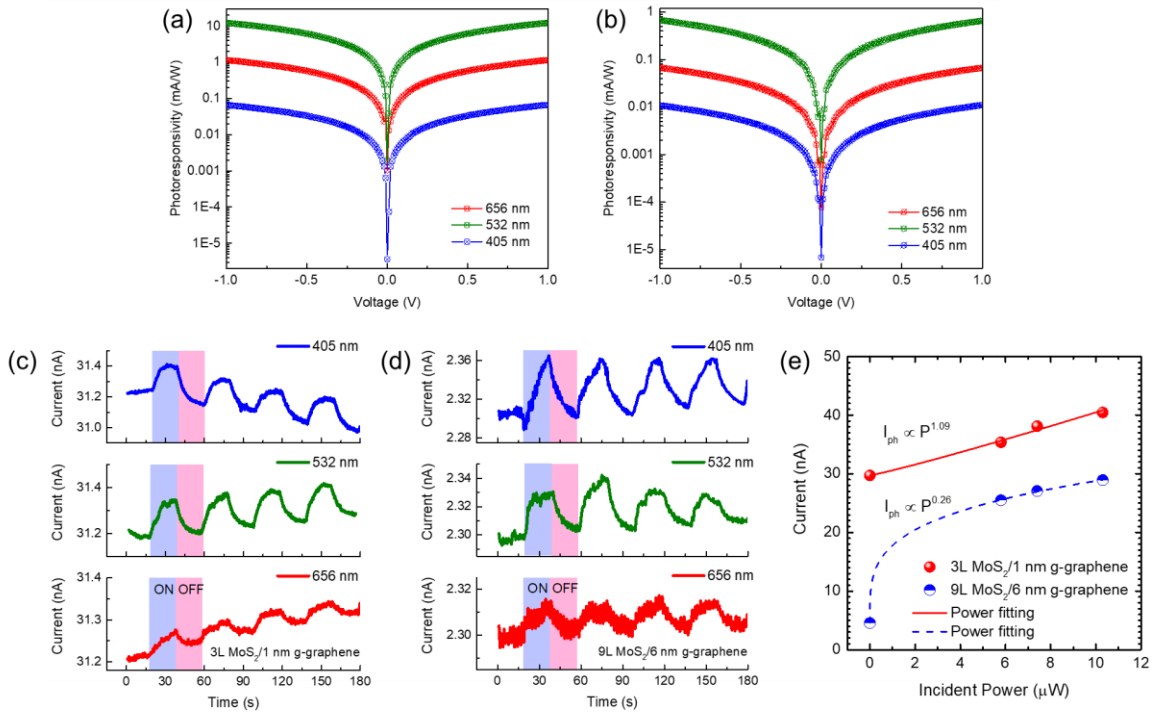
(a)
Photoresponsivity (mA/W)
Voltage (V)
656 nm
532 nm
405 nm
(b)
Photoresponsivity (mA/W)
Voltage (V)
656 nm
532 nm
405 nm
(c)
405 nm
532 nm
656 nm
ON OFF
3L MoS2/1 nm g-graphene
Current (nA)
Time (s)
(d)
405 nm
532 nm
656 nm
ON OFF
9L MoS2/6 nm g-graphene
Current (nA)
Time (s)
(e)
Iph ∝ P1.09
Iph ∝ P0.26
3L MoS2/1 nm g-graphene
9L MoS2/6 nm g-graphene
Power fitting
Power fitting
Current (nA)
Incident Power (μW)

The table of contents entry:

Transparent photodetectors based on a novel few-layer MoS_2/glassy-graphene heterostructure are reported for the first time, which exhibit high detectivity and distinct wavelength selectivity. It is demonstrated that ohmic contact is formed at the heterojunction. Density functional theory calculations reveal the band alignment of the layered heterostructures can be manipulated by lattice engineering of 2D nanosheets to enhance optoelectronic performance.

Keywords: glassy-graphene, MoS_2, heterostructures, photodetectors, density functional theory

Hao Xu, Xiaoyu Han, Xiao Dai, Wei Liu, Jiang Wu*, Juntong Zhu, Dongyoung Kim, Guifu Zou*, Kimberley A. Sablon, Andrei Sergeev, Zhengxiao Guo, Huiyun Liu*

Title: High Detectivity and Transparent Few-layer MoS_2/Glassy-Graphene Heterostructure Photodetectors

ToC figure: